Monthly Notices of the ROYAL ASTRONOMICAL SOCIETY

MNRAS **475,** 999–1009 (2018) doi:10.1093/mnras/stx3121
Advance Access publication 2017 December 1

Changes in the pulse phase dependence of X-ray emission lines in 4U 1626−67 with a torque reversal

Aru Beri,[1,2]★† Biswajit Paul[1] and Gulab C. Dewangan[3]

[1]*Raman Research Institute, Sadashivnagar, C. V. Raman Avenue, Bangalore 560 080, Karnataka, India.*
[2]*School of Physics and Astronomy, University of Southampton, Southampton, Hampshire SO17 1BJ, UK*
[3]*Inter University Centre for Astronomy and Astrophysics, Post bag 4, Ganeshkhind, Pune 411007, Maharashtra, India*

Accepted 2017 November 29. Received 2017 November 29; in original form 2016 December 4

ABSTRACT

We report results from an observation with the *XMM–Newton* observatory of a unique X-ray pulsar 4U 1626−67. European Photon Imaging Camera-pn data during the current spin-up phase of 4U 1626−67 have been used to study pulse phase dependence of low-energy emission lines. We found strong variability of low-energy emission line at 0.915 keV with the pulse phase, varying by a factor of 2, much stronger than the continuum variability. Another interesting observation is that behaviour of one of the low-energy emission lines across the pulse phase is quite different from that observed during the spin-down phase. This indicates that the structures in the accretion disc that produce pulse phase dependence of emission features have changed from spin-down to spin-up phase. This is well supported by the differences in the timing characteristics (like pulse profiles, quasi periodic oscillations, etc.) between spin-down and spin-up phases. We have also found that during the current spin-up phase of 4U 1626−67, the X-ray pulse profile below 2 keV is different compared to the spin-down phase. The X-ray light curve also shows flares which produce a feature around 3 mHz in power density spectrum of 4U 1626−67. Since flares are dominant at lower energies, the feature around 3 mHz is prominent at low energies.

Key words: pulsars: individual: 4U 1626−67.

1 INTRODUCTION

4U 1626−67 is a remarkable ultracompact X-ray binary bearing a neutron star with a pulse period of 7.7 s (Rappaport et al. 1977). Evidence of binary motion has never been revealed from X-ray timing measurements (see e.g. Rappaport et al. 1977; Joss, Avni & Rappaport 1978; Jain et al. 2008). An orbital period of 42 min has been inferred from the pulsed optical emission reprocessed on the surface of secondary (Middleditch et al. 1981; Chakrabarty 1998). An upper limit of 10 lt-ms for pulse arrival delay has been reported by Jain et al. (2008) using X-ray data from *RXTE*-PCA. Time-scale of torque reversals observed in most of the accretion powered pulsars varies from weeks to months and years and, in most cases, accretion torques are often related to the X-ray luminosity. 4U 1626−67, a persistent X-ray source, underwent two torque reversals since its discovery (Camero-Arranz et al. 2010). It was initially observed in spin-up state; this trend reversed in 1990 and the neutron star began to spin-down. After the steady spin-down phase of about 18 years, a transition to spin-up took place in 2008. The second torque reversal was detected with *RXTE*-PCA (Jain & Paul 2009) and *Fermi*-GBM (Camero-Arranz, Finger & Wilson 2009). Moreover, it is observed that this source does not obey standard X-ray luminosity–accretion torque relation (Beri et al. 2014). X-ray features during spin-down phase were different in comparison with both spin-up phases. The most outstanding difference in energy resolved pulse profiles of the two spin-up eras and the spin-down era was disappearance of the sharp double-peaked profile during spin-down era (for details, see Beri et al. 2014). Quasi periodic oscillation (QPO) at 48 mHz was observed in all the observations during spin-down phase (Kaur et al. 2008); this feature was absent in the power density spectra (PDSs) created using X-ray data during current spin-up phase (Jain, Paul & Dutta 2010).

The X-ray spectrum of 4U 1626−67 is well described using two continuum components: a hard power law and a blackbody. X-ray spectra during both spin-up phases showed a blackbody temperature of about 0.6 keV while during the spin-down phase of 4U 1626−67 the blackbody temperature decreased to ∼0.3 keV. Moreover, the energy spectrum became harder during the spin-down phase. The power-law photon index showed a value of ∼1.5 during the first spin-up phase which changed to ∼0.4–0.6 during the spin-down phase and during the second spin-up phase it showed a value in the range of 0.8–1.0 (see Beri et al. 2014, references therein). Detailed

★ E-mail: a.beri@soton.ac.uk
† Royal Society–SERB Newton International Fellow.

study of this source during each phase of torque reversal suggests that accretion flow geometry is different during the spin-up and spin-down phases and plays an important role in transfer of angular momentum (Jain et al. 2010; Beri et al. 2014).

X-ray spectrum of 4U 1626−67 is unique, unusually bright neon (Ne) and oxygen (O) lines have been reported from many spectroscopic observations (Angelini et al. 1995; Owens, Oosterbroek & Parmar 1997; Schulz et al. 2001; Krauss et al. 2007). Observations made with *Chandra* revealed double-peaked nature of low-energy emission line features, indicating their formation in the accretion disc (Schulz et al. 2001). Continuum of the spectra is well described using a soft emission component and a power law (see Beri, Paul & Dewangan 2015, and references therein) though.

Observations made during spin-down and spin-up phases of 4U 1626−67 with the *Suzaku* observatory were used to measure spectral changes with torque reversal in 2008 (Camero-Arranz et al. 2012). The authors confirmed that the equivalent width (EW) and the intensity of these emission lines are variable. They found that fluxes of all the emission lines have increased almost by a factor of ∼5 with an exception of Ne X (1.02 keV) emission line that showed an increase by a factor of ∼8 after the torque reversal. Pulse-phase-resolved spectroscopy performed using data from the *XMM–Newton* observatory during the spin-down phase of 4U 1626−67 revealed that line fluxes show pulse phase dependence (Beri et al. 2015) One of the emission lines (O VII) showed the line flux to vary by a factor of about 4, significantly larger compared to the relative variation of total flux. Warp-like structures in the accretion disc are believed to be the cause of observed line flux variability.

An interesting possibility for the cause of spin-down is the radiation pressure induced warping of the inner accretion disc which may become retrograde leading to negative accretion torque (van Kerkwijk et al. 1998). Moreover, changes in the timing characteristics (like the pulse profile, the QPOs, etc.) in the spin-down phase compared to spin-up phase are understood to be due changes in the inner accretion flow from a warped accretion disc in the spin-down phase. Therefore, we expect to observe changes in the accretion flow and probably also the accretion disc structures of 4U 1626−67 during the spin-up phase. We carried out a pulse-phase-resolved spectroscopy to investigate if this results into a different modulation of the emission lines during its current spin-up phase. In this paper, we present results obtained from timing and spectral study of 4U 1626−67, performed using data obtained with the *XMM–Newton* observatory during its current spin-up phase. The paper is structured as follows. We describe observation details and data reduction procedure in Section 2. This is followed by the results from timing analysis (Section 3). In Section 4, we present results from the spectral analysis. In Section 5, we present results and discussions.

2 OBSERVATIONS AND DATA REDUCTION

We have obtained a 56 ks observation of 4U 1626−67 during its current spin-up phase with *XMM–Newton*. The observation was performed on 2015 October 5 bearing an ID-0764860101.

XMM–Newton satellite has three X-ray telescopes, each with a European Photon Imaging Camera (EPIC) at the focus (Jansen et al. 2001). Two of the EPIC imaging spectrometers use metal-oxide semiconductors (MOS) CCDs (Turner et al. 2001) and one used pn CCD (Strüder et al. 2001). Reflection grating spectrometer (RGS) and optical monitor (OM) are two other instruments onboard the *XMM–Newton* satellite. RGS comprises two spectrometers, namely RGS1 and RGS2. Two RGSs have a bandpass of 0.35–2.5 keV and first-order spectral resolution of about 200–800 in 0.35–2.5 keV. They are attached to two of the X-ray telescopes with MOS. Simultaneous optical/UV observations are carried out with the OM.

In this work, we performed analysis using data from the EPIC-pn and the RGS onboard *XMM–Newton*. EPIC-pn data were collected in a timing mode using a medium filter with a frame time of 6 ms. In the timing mode, only one CCD chip is in operation and data are collapsed into a one-dimensional row and read out at high speed. RGS data were operated in standard a 'spectral' mode.

We processed the *XMM–Newton* observation data files, using the science analysis software (SAS version 15.0). Latest updated calibration files available as on 2016 April were applied.

Standard SAS tool EPPROC was used to obtain EPIC-pn event file. We first checked for flaring particle background in the data. A light curve was extracted using a selection criterion: PATTERN=0 in the energy range of 10–12 keV. We found no evidence of soft proton flaring. Thereafter, we extracted EPIC-pn cleaned event list by selecting events with PATTERN≤4, FLAG=0 and energy in the range 0.3–12 keV. This cleaned event file was used to extract source events and background files. We used a rectangular box with RAWX = 30–46 for source events and RAWX = 2–4 for background. Source event file was also checked for photon pile-up using SAS tool EPATPLOT. No significant photon pile-up was found. Barycentre correction was performed using SAS tool BARYCEN. For extraction of light curves and spectra, SAS tool EVSELECT was used. Response matrix and ancillary response files were generated using the SAS task RMFGEN and ARFGEN, respectively.

For the RGS data reduction, we used SAS tool RGSPROC to reduce and extract calibrated source and background spectrum and response files. Standard procedure as mentioned in SAS analysis thread was followed.

3 TIMING ANALYSIS

The left-hand side of Fig. 1 shows barycentre corrected and background subtracted light curve of 4U 1626−67 obtained using the EPIC-pn data. Light curve is highly variable. It includes both flares and dip features in it. X-ray flares have also been observed in the light curves created using previous observations made during its spin-up phase (see Beri et al. 2014, and references therein). Amplitude of flares is 2–3 times above the persistent level (Fig. 1). Duration of flares is few hundred of seconds. Recurrence time-scales of these flares vary between 300 and 1000 sand these time-scales are consistent with the previous reports (see Joss et al. 1978; Li et al. 1980; Raman et al. 2016).

Unlike other flaring sources like LMC X–4 and SMC X−1, where persistent emission begins just after the end of flares, it is interesting to notice a sharp dip in the light curve near the decay of bright flares at 18 000, 23 000 s (second panel), and 51 000 s (fourth panel) of Fig. 1. This feature has never been reported before in 4U 1626−67. Similar kind of dip near the end of outburst has also been observed in the light curves of bursting pulsar (GRO J1744-28; e.g. Giles et al. 1996).

3.1 Power density spectrum

PDS generated using the EPIC-pn light curve is shown in Fig. 1. The light curve was divided into stretches of 8192 s. PDSs from all the segments were averaged to produce the final PDS and were normalized such that their integral gives squared rms fractional variability and the white noise level was subtracted. PDS showed a narrow peak at around 0.130 Hz which corresponds to the spin frequency of the neutron star. Multiple harmonics are also seen

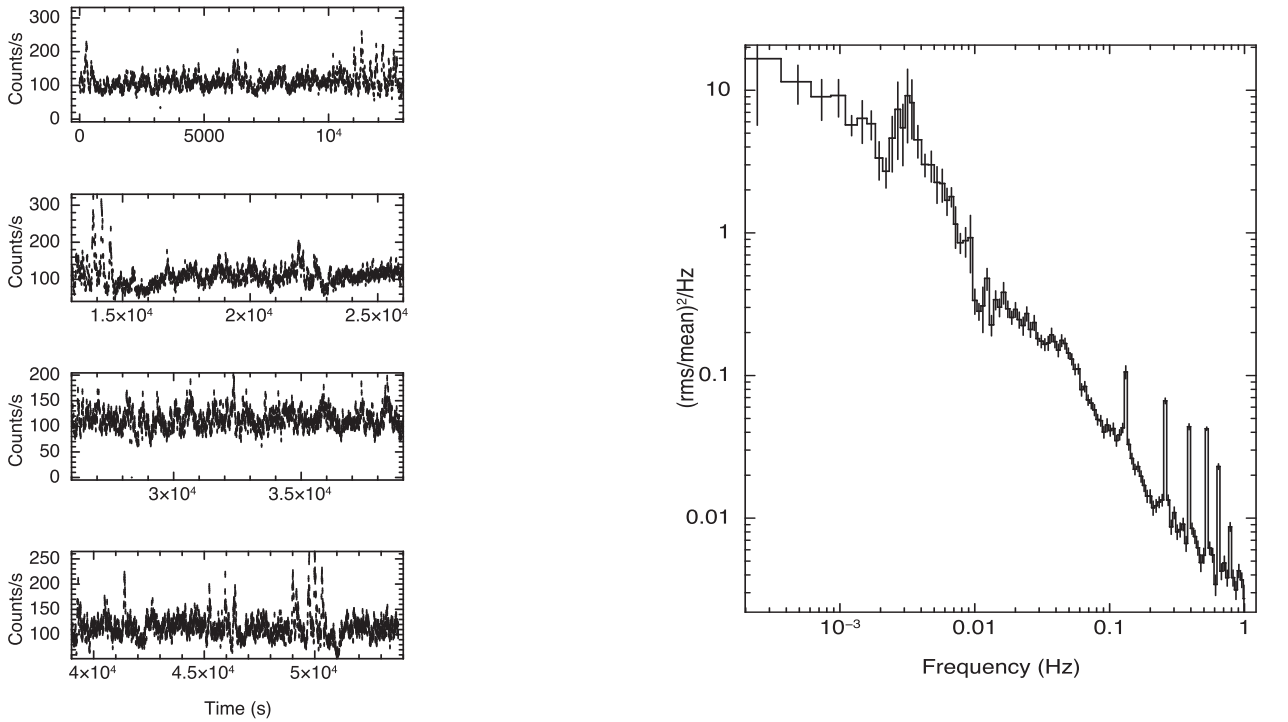

Figure 1. Light curves in the 0.3–12 keV band of 4U 1626−67, created using data from EPIC-pn onboard *XMM–Newton*, are shown in left. We divided data into four short segments each of ∼14 ks for visual clarity of flares. Light curves are binned using 7.7 s. In the right, we show power density spectrum (PDS) created using the same light curve.

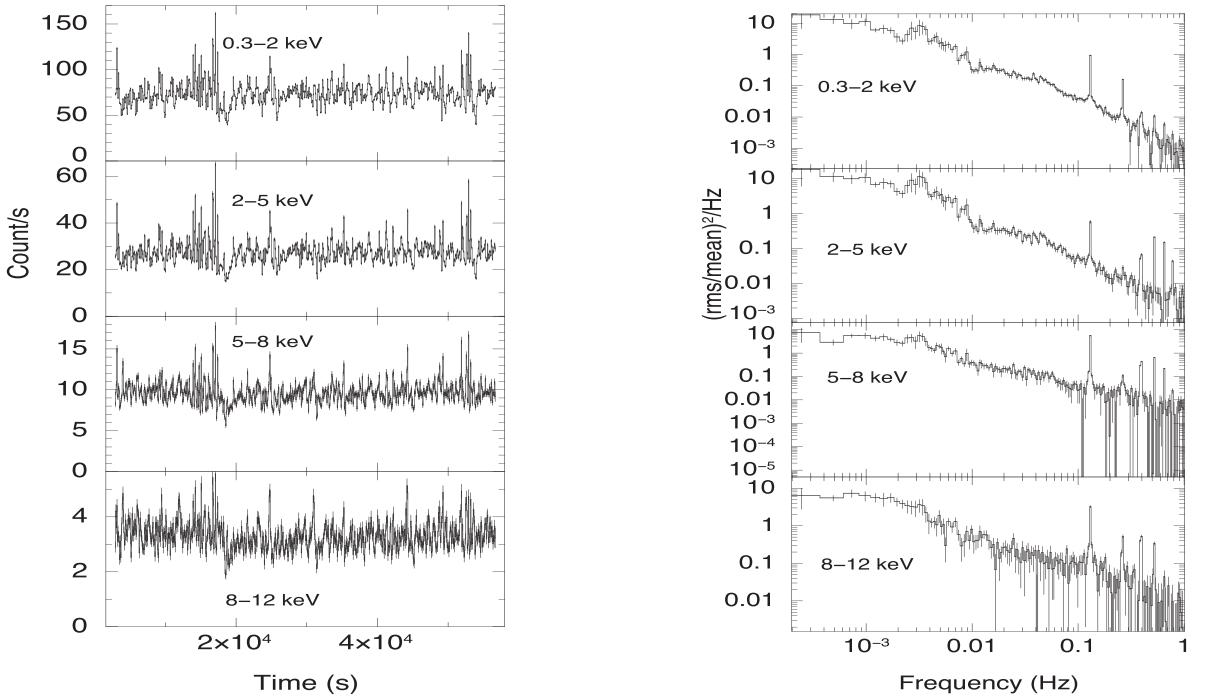

Figure 2. Energy resolved light curves binned with 77 s are shown in left. These light curves were used to generate PDSs, shown in the right. This plot shows a QPO feature at ∼3 mHz and some energy dependence of PDS of 4U 1626−67.

in the PDS of the source. In addition to the main peak, a QPO feature is seen at ∼3 mHz with fractional rms amplitude of ∼7.26 ± 0.07 per cent. 3 mHz QPO can be due to flares seen in the light curve and this feature is observed for the first time in the X-ray data during current (spin-up) phase of 4U 1626−67. A similar mHz QPO was however observed in the PDS generated with X-rays during the first spin-up phase of 4U 1626−67 (see e.g. Joss et al. 1978). Another interesting observation is dependence of a 3 mHz QPO on energy (Fig. 2). It is evident from Fig. 2 that flares are more prominent at lower energies and therefore a sharp feature in the PDS around 3

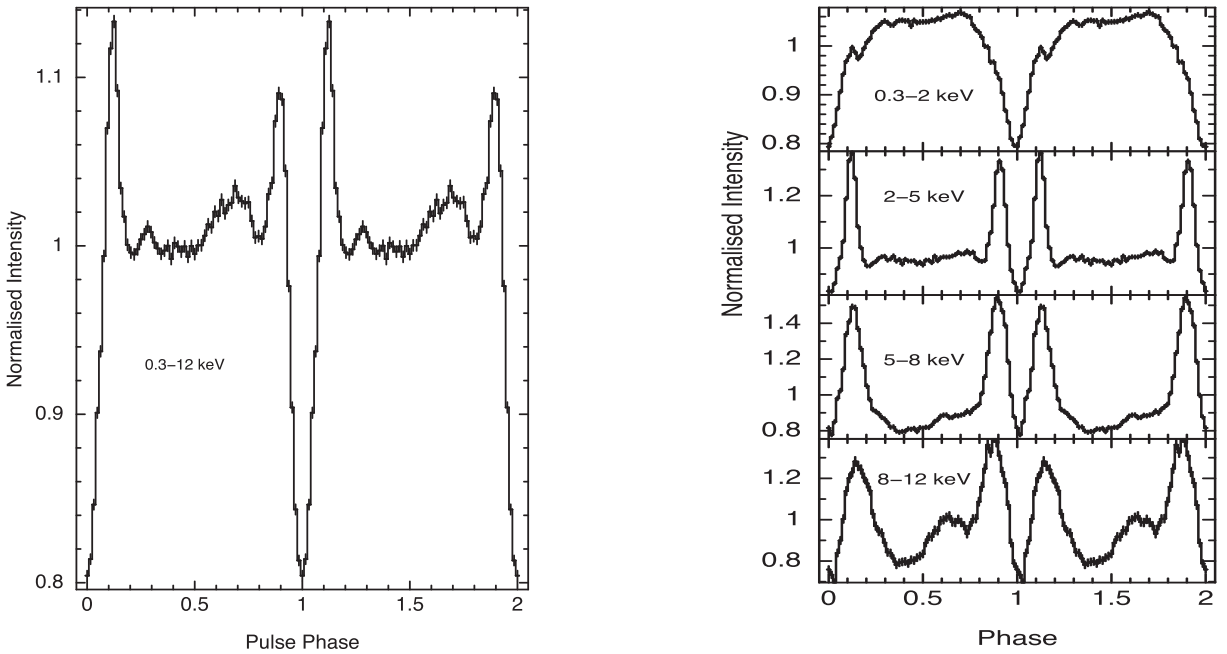

Figure 3. Left: the average pulse profile created in the energy band 0.3–12 keV. Right: the energy resolved pulse profiles. Pulse profiles are binned into 64 phase bins.

mHz is dominant at energies below 5 keV. Fractional rms amplitudes of a 3 mHz QPO feature in the PDS created using light curves in different energy bands, namely 0.3–2 keV, 2–5 keV, 5–8 keV, and 8–12 keV are 7.8 ± 0.1 per cent, 9.4 ± 0.4 per cent, 4 ± 2 per cent, and 4 ± 2 per cent, respectively. We also detect a signature of broad QPO around 48 mHz with rms amplitude of $\sim$5 per cent, much smaller than the rms in the 48 mHz QPO seen during the spin-down phase (e.g. Kommers, Chakrabarty & Lewin 1998).

3.2 Pulse profiles

Spin-period was determined to be $7.672\,55 \pm 0.000\,09$ s using epoch folding χ^2 maximization technique. This period was used for creating pulse profiles. We first created an average pulse profile with 64 phase bins, using light curve in the 0.3–12 keV energy band (Fig. 3). The bi-horned peaks observed in the pulse profiles look similar to the previously reported pulse profiles of 4U 1626−67 during its spin-up era (see e.g. Beri et al. 2014). However, in the 0.3–12 keV band, amplitude of first peak is slightly small compared to the second peak.

The energy resolved pulse profiles were created using the light curves in the energy bands of 0.3–2 keV, 2–5 keV, 5—8 keV, and 8–12 keV. Thanks to *XMM–Newton* which enabled us to investigate pulse profiles below 2 keV during its current spin-up phase for the first time. Pulse profile in the 0.3–2 keV band looks simple having a shoulder-like structure. It has a sharp dip around phase 0.0. It seems that the sharp dip observed in the 0.3–2 keV profiles mainly contributes to the dip observed between the two horns in the energy averaged profiles (0.3–12 keV). Profile shape in the 0.3–2 keV band is similar to that seen during the first spin-up phase (Pravdo et al. 1979). It is interesting to see that pulse profile below 2 keV is quite different from that observed in other energy bands. This suggests that pulsation of a soft component is different from that in higher energy band pulse profiles which indicate that pulsation of a thermal component is different from a power-law component. A soft spectral component that pulsates differently from the power-law component has been detected in other sources with low absorption column density (e.g. SMC X−1 and LMC X−4) and has been interpreted as reprocessed thermal emission from the inner accretion disc (Paul et al. 2002).

To compare pulse profiles below 2 keV during its current phase with that of the spin-down phase, we created pulse profile in the energy band of 0.3–2 keV using data from previous *XMM–Newton* observation (ObsID-0152620101) during its spin-down phase. We performed data reduction and analysis in the same way as discussed in our previous paper on 4U 1626−67 (Beri et al. 2015). It is interesting to see that pulse profile during spin-down phase is quite different from that during its current phase. Pulse profile below 2 keV has many structures during spin-down phase which is not the case during its current spin-up phase (see Fig. 4). Pulse profiles in remaining energy bands are consistent with previous observations in spin-up state (see Beri et al. 2014, and references therein).

4 SPECTROSCOPY

4.1 Phase-averaged spectroscopy

We performed simultaneous spectral fitting, using data from RGS and EPIC-pn (Fig. 5). Spectra of first order obtained using RGS1 and RGS2 were grouped using the tool GRPPHA (HEASOFT *Version*-6.17) to contain six channels per bin. We have used the 0.35–1.8 keV band of RGS for spectral fitting. Mean spectrum extracted using EPIC-pn was rebinned using the SAS task SPECGROUP to oversample the full width at half-maximum of energy resolution by a factor of 3 and to obtain minimum of 25 counts/bin. There is no reliable calibration below 0.7 keV for EPIC-pn in timing mode[1] and the disagreement between the EPIC-pn and the RGS is larger below 0.7 keV. Therefore, we have used the 0.8–12 keV band of EPIC-pn for spectral fitting. All the spectral parameters other than

[1] http://xmm2.esac.esa.int/docs/documents/CAL-TN-0018.pdf

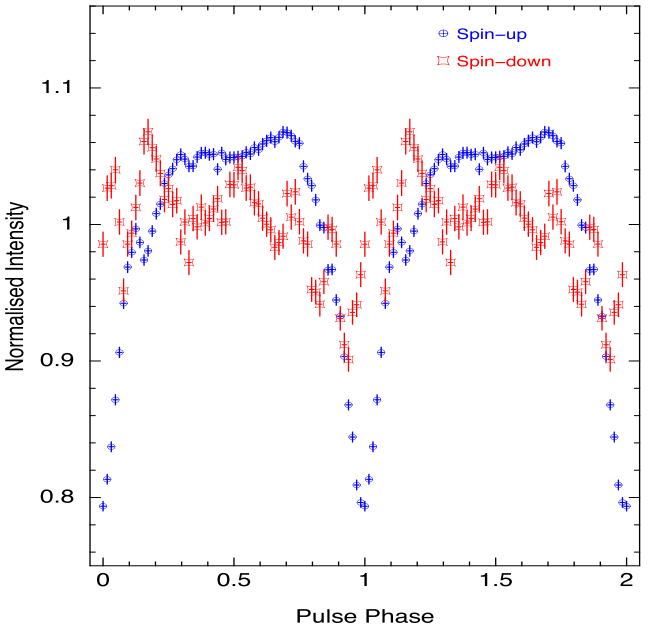

Figure 4. Pulse profile created in the energy band of 0.3–2 keV using *XMM–Newton*-pn data of spin-down is shown in red. This figure demonstrates that pulse profile below 2 keV is quite different from that seen in the current spin-up phase (blue).

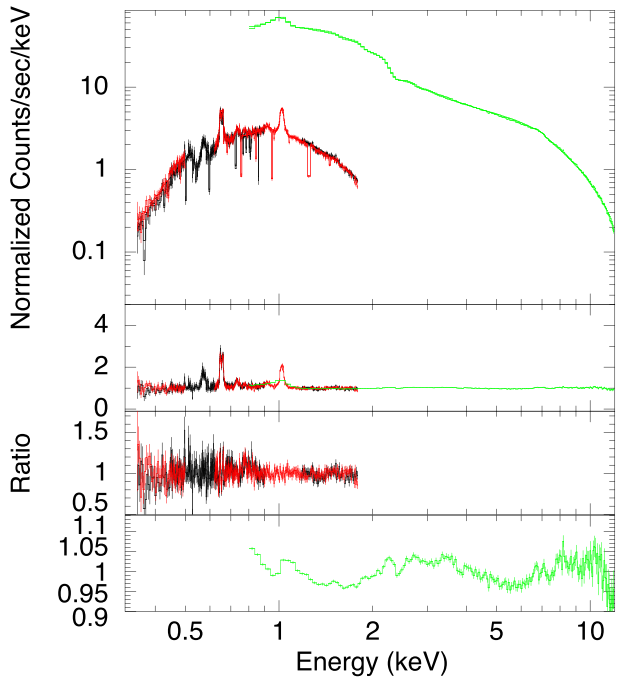

Figure 5. Best-fittingphase-averaged spectrum obtained after performing simultaneous fit of RGS and EPIC-pn data. Second panel shows the ratio plot obtained after adding only continuum components while bottom two panels show the ratio plots of pn and RGS, respectively, obtained after the best fit.

the relative instrument normalization were tied together for both RGS and EPIC-pn. We fixed the instrumental normalization of RGS1 to 1, and freed the normalization of the RGS2 and EPIC-pn instruments. The values of CONSTANT model component obtained for RGS2 and EPIC-pn are 0.977 ± 0.007 and 1.04 ± 0.01, respectively. A blackbody component and a power law well describes the continuum of the phase-averaged spectrum (Pravdo et al. 1979; Kii et al. 1986; Angelini et al. 1995; Owens et al. 1997; Orlandini et al. 1998; Schulz et al. 2001; Krauss et al. 2007; Jain et al. 2010; Iwakiri et al. 2012). Therefore, we modelled the continuum of the spectrum using *tbabs*(bbodyrad+powerlaw)*. Using only the continuum model showed a significant excess in the residuals in the form of emission lines. The second panel of Fig. 5 shows the ratio between data and model, indicating the presence of low-energy emission lines (below 1 keV). The raw RGS spectrum shows the presence of two strong emission lines around 0.65 and 1.0 keV; therefore, we added two Gaussian components around 0.65 and 1.0 keV. These line energies correspond to Ne X and O VIII. Adding these two Gaussian components was not adequate to obtain a good spectral fit. The presence of additional emission features at 0.73, 0.571, and 0.913 keV was observed in the residuals of the RGS data. The presence of O VII and Ne IX emission lines around 0.569 and 0.915 keV, respectively, in the X-ray spectrum of 4U 1626−67 has been reported earlier by several authors (see e.g. Schulz et al. 2001; Krauss et al. 2007). Therefore, to obtain an appropriate fit, we added two additional Gaussian components at these line energies. However, we required an additional Gaussian component to model the excess seen around 0.73 keV. This line energy corresponds to an iron (Fe-L shell) emission feature. Table 1 shows the best-fitting parameters obtained. They are consistent with the previous results

Table 1. Best-fitting parameters obtained from simultaneous fit of RGS1, RGS2, and pn spectrum.

Parameter	Model values
$N_{\rm H}$ (10^{22} atoms cm^{-2})	0.085 ± 0.003
$kT_{\rm bbodyrad}$(keV)	0.427 ± 0.005
PowIndex (Γ)	0.914 ± 0.014
$N_{\rm PL}^{a}$	0.0229 ± 0.0006
Line energy[b]	
O VII	0.571 ± 0.001
O VIII	0.6536 ± 0.0003
Ne IX	0.913 ± 0.004
Ne X	1.022 ± 0.001
Fe(L shell)	0.733 ± 0.001
Fe(K shell)	6.8 ± 0.1
Line width[c]	
O VII	0.009 ± 0.001
O VIII	0.0075 ± 0.0002
Ne IX	0.035 ± 0.005
Ne X	0.0115 ± 0.0006
Fe(L shell)	0.009 ± 0.002
Fe(K shell)	0.14 ± 0.09
Line flux[d]	
O VII	11 ± 1.0
O VIII	25.0 ± 1.0
Ne X	13 ± 1.0
Ne X	23.0 ± 1.0
Fe(L shell)	7.0 ± 0.7
Fe(K shell)	0.6 ± 0.3
Reduced χ^2	1.43(dof 1337)

Note: Errors quoted are with 90 per cent confidence range. Energy range used is 0.35–1.8 keV for RGS1 and RGS2 and 0.8–12.0 keV for EPIC-pn.
[a]Power-law normalization ($N_{\rm PL}$) is in units of photons cm^{-2} s^{-1} keV^{-1} at 1 keV.
[b]Line energy in units of keV.
[c]Line width in units of keV.
[d]Gaussian normalization is in units of 10^{-4} photons cm^{-2} s^{-1}.

during spin-up phase of 4U 1626−67 (see e.g. Camero-Arranz et al. 2010). The EWs of O VII (0.571 keV), O VIII (0.653 keV), Fe-L shell (0.73 keV), Ne IX (0.913 keV), and Ne X (1.02 keV) emission lines are 17.0 ± 1.0 eV, 34 ± 2 eV, 9.0 ± 1.0 eV, 20 ± 3.0 eV, and 42.0 ±1 eV, respectively.

Here, we emphasize that for the first time the X-ray spectrum of 4U 1626−67 showed an Fe-L shell fluorescence emission feature and the detection of this feature at 0.73 keV is statistically significant as the value of chi-square (χ^2) increased from 2049 to 2458 (1341 degrees of freedom) on fixing its normalization to zero. A systematic error of 2 per cent was added quadratically to each energy bin to account for all the artefacts due to calibration issues in the EPIC-pn timing mode data. The residuals of EPIC-pn showed the presence of a weak iron fluorescence emission line around 6.8 keV. Therefore, we added another Gaussian component with line energy centred around 6.8 keV to the spectrum. The EW of the emission line observed at 6.8 keV is ∼0.02 ± 0.01 keV. The spectral fit resulted into reduced χ^2 (χ^2_ν) of 1.43 for 1337 degrees of freedom (see Table 1). We also observed that fixing the normalization of Fe K shell line to zero leads to an increase in the value of chi-square (χ^2) from 1914 to 1930 (1338 degrees of freedom) which suggests that the detection of this emission feature is statistically significant. The presence of Fe K_α emission line was also observed in the MOS 2 spectrum. The values of line flux and the EW observed in the MOS 2 data are $0.58^{0.5}_{-0.3} \times 10^{-4}$ photons cm^{-2} s^{-1} and 0.015 ± 0.010 keV, respectively. These values are similar to that observed in the pn data and on fixing the normalization to zero of this line in the MOS 2 data also showed increase in the value of chi-square (172–183 for 171 degrees of freedom) which is similar to that observed in the pn data. The addition of the systematic error to the pn data is not likely to introduce any pulse phase dependence of emission line fluxes which is the main motivation of this work. Here, we would like to mention that owing to limited statistical significance of Fe K_α emission line we have not performed phase-resolved spectroscopy for this line.

It is believed that Ne/O emission lines observed in the X-ray spectra of 4U 1626−67 originate from highly ionized layers of the accretion disc. The existence of double-peaked profiles supports their disc origin (Schulz et al. 2001; Krauss et al. 2007). Interestingly, we noticed that one of the emission lines at 0.653 keV (O VIII) showed the presence of double-peaked profiles in the high-resolution data of RGS (Fig. 6). Therefore, we fit this line with a pair of Gaussian to resolve into the Doppler pairs and to estimate the disc velocities of red and blueshifted components. The line velocities measured using the RGS data along with the previous known values are given in Table 2. The single-Gaussian fit revealed a broad emission line at 1.02 keV (Ne X) in the RGS2 spectrum. Therefore, we fit this line as well with a pair of Gaussian, and the velocities measured are given in Table 2. Ne IX emission line observed in the *XMM–Newton* data did not allow us to measure Doppler velocities.

4.2 Pulse-phase-resolved spectroscopy

For performing pulse-phase-resolved spectroscopy, we have used data from EPIC-pn. We added 'PHASE' column to the pn event list. This was performed using SAS task PHASECALC with phase zero fixed at the reference time (epoch) used for creating pulse profiles. Thereafter, appropriate good time intervals (GTI) files were created for narrow phase bins of 0.05. These GTI files were used for the extraction of 20 phase-resolved source spectra. Response matrices and ancillary response files used for phase-averaged spectroscopy were used again for performing phase-resolved spectroscopy. Spectral fitting was done in the energy range of 0.8–12 keV with the same spectral model consisting of a power law, a blackbody, and several emission lines. We fixed the neutral hydrogen column density, line energies, and line widths to the values obtained from the phase-averaged spectrum. The left plot of Fig. 7 shows variation of flux of low-energy emission lines with pulse phase. From the plot, we observe:

(i) Ne IX He_α emission line at 0.913 keV shows strong variation with pulse phase (a factor of ∼2.0 ± 0.3). χ^2 value of 103 for 20 phase bins was observed after fitting a constant to the flux of line at 0.913 keV.

(ii) Ne X Ly α emission line at 1.02 keV shows no significant variation with pulse phase. This is similar to the previous observations made during spin-down phase of 4U 1626−67 (Angelini et al. 1995; Beri et al. 2015). A constant fitted to the flux of Ne X Ly α emission line showed a χ^2 value of 32 for 20 phase bins.

We estimated the observed total continuum flux in the energy band of 0.7–12 keV, *power-law* flux in the 2–12 keV band, and the *blackbody* flux in the 0.7–2 keV band using the CFLUX convolution model in XSPEC. The continuum flux profile plotted in the right-hand side of Fig. 7 shows that the modulation of the *power law* is same as the modulation of the total flux while the flux modulation of the *blackbody* component has a different shape. The blackbody component shows a broad dip, consistent with the pulse profile in the 0.3–2.0 keV band in which the blackbody component dominates. Shape of the power-law profile can be imagined to have formed as a narrow dip at the centre of a broad pulse peak, while the blackbody profile is a broad dip on an otherwise constant emission.

Continuum parameters also showed variation with pulse phase (Fig. 8). Blackbody temperature shows strong variation with possible correlation with the pulse profile. However, blackbody normalization profile shape is anticorrelated to its temperature profile. Power-law index profile shows a sharp dip at phase 0.2 with some structures in rest of the profile while power-law normalization shows a strong correlation with the pulse profile shape (bi-horned peaks around pulse phase 0.9 and 1.1). The blackbody flux is a few per cent of the total flux and given the systematic errors in EPIC-PN, one should be cautious about the blackbody parameters. The flux modulation of the blackbody is however certainly different from the power-law flux variation, as is evident from the energy-resolved pulse profiles.

4.3 Intensity-resolved spectroscopy

Since strong variation in count rates is observed in light curve shown in Fig. 1, we extracted intensity-resolved spectra from EPIC-pn data using SAS task EVSELECT. GTIs were created in different intensity ranges: a sharp dip seen just after the end of first flare seen in Fig. 1 and pn count rates between 90 and 150 counts s^{-1}, 150 and 200 counts s^{-1}, and 200 and 320 counts s^{-1} were used to extract intensity-resolved spectra. For spectral fitting, we used the same technique which we opted while performing phase-resolved spectroscopy. Neutral hydrogen column density, line energies, and widths were fixed to the phase-averaged values. We also added 2 per cent systematics while performing the spectral fitting. Fitted model components are shown in Fig. 9. The temperature of blackbody and the power-law index were found to increase. The line fluxes and fractional contribution of the blackbody flux were also found to increase with total flux (Fig. 10).

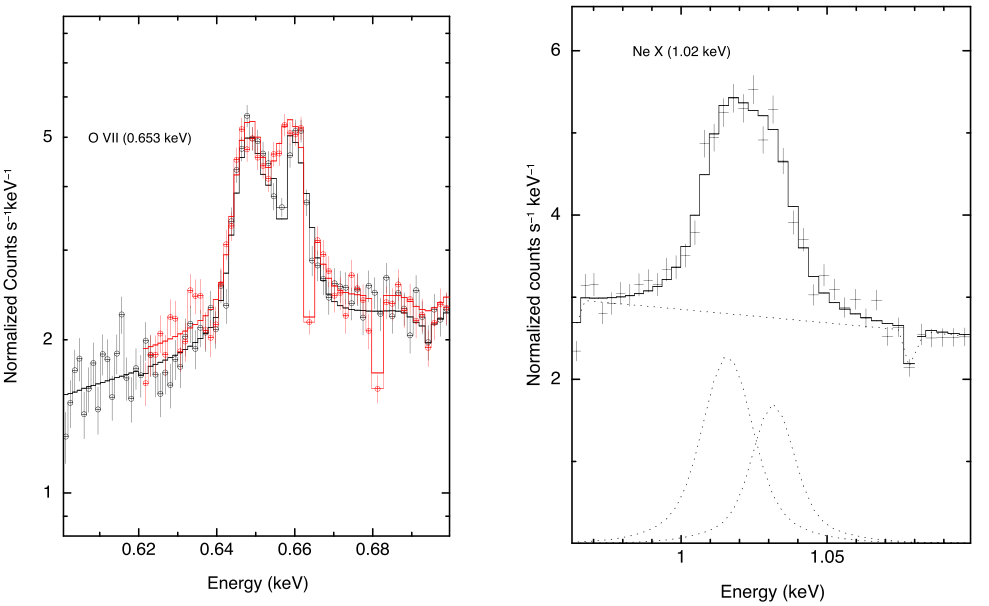

Figure 6. Double-peaked emission lines. Left: the hydrogenic O VIII emission line observed with RGS-1 and 2. Right plot shows the broad hydrogenic Ne X emission line as observed with the RGS-2 data.

Table 2. Double-Gaussian emission line fits.

Observatory	MJD	Blueshifted lines		Redshifted lines		Reference
		V (kms^{-1})	Flux[a]	V (kms^{-1})	Flux[a]	
			O VIII (0.653 keV)			
Chandra	51803.6	1740 ± 440	14.04 ± 2.52	1900 ± 480	17.82 ± 0.57	Schulz et al. (2001)
XMM–Newton	52145.1	1930 ± 260	$17.6^{4.7}_{-4.4}$	1930 ± 260	$21.9^{+4.9}_{-4.5}$	Krauss et al. (2007)
Chandra	52795.1	1770 ± 330	$13.0^{+5.7}_{-4.9}$	1770 ± 330	$13.7^{+5.8}_{-5.0}$	Krauss et al. (2007)
XMM–Newton	52871.2	1810 ± 180	$12.7^{+2.1}_{-1.9}$	1810 ± 180	$12.4^{+2.0}_{-1.8}$	Krauss et al. (2007)
XMM–Newton	56397	1535 ± 158	71 ± 6	1306 ± 158	61 ± 6	This work
			Ne X (1.02 keV)			
Chandra	51803.6	2220 ± 350	8.15 ± 0.93	1240 ± 220	15.04 ± 1.65	Schulz et al. (2001)
XMM–Newton	52145.1	1910 ± 450	$11.1^{+4.8}_{-4.6}$	1910 ± 450	$14.4^{-3.4}_{-5.2}$	Krauss et al. (2007)
Chandra	52795.1	1670 ± 180	$8.2^{+1.4}_{-1.5}$	1670 ± 180	$10.5^{+1.8}_{-1.6}$	Krauss et al. (2007)
XMM–Newton	52871.2	1780 ± 420	$11.3^{2.6}_{-2.6}$	1780 ± 420	$9.0^{2.5}_{-2.6}$	Krauss et al. (2007)
XMM–Newton	56397	1731 ± 247	65 ± 20	1484 ± 247	98 ± 22	This work

Note.[a] The Gaussian normalization is in units of 10^{-5} photonscm^{-2} s^{-1}.

5 DISCUSSION AND SUMMARY OF RESULTS

In this paper, we present results obtained using data from the *XMM–Newton* observatory during the current spin-up phase of 4U 1626−67. Several new and significant changes have been observed in comparison to the previous observation made during its spin-down phase. The main focus of our study is to observe a pulse phase dependence of low-energy emission lines seen in the X-ray spectrum of 4U 1626−67. Strong pulse phase dependence of O VII emission line at 0.569 keV was observed during the spin-down phase of 4U 1626−67. This strong variation was interpreted as a result of warps in the accretion disc (Beri et al. 2015). Dissimilarities in timing characteristics (such as pulse profile, QPOs) during spin-down and spin-up eras are believed to be due to difference in the inner accretion flow from a warped accretion disc during the spin-down phase (Kaur et al. 2008; Beri et al. 2014). Therefore, one expects to see a different behaviour of line fluxes with pulse phase during current spin-up phase of this source. The calibration issues below 0.7 keV in the timing mode data of EPIC-pn did not allow us to study the pulse phase dependence of emission line features at 0.571 keV (O VII), 0.653 keV (O VIII), and 0.733 keV (Fe L). However, we investigated the behaviour of emission lines at 0.913 keV (Ne IX) and 1.02 keV (Ne X) with the pulse phase.

We summarize the results as follows:

(i) Light curve obtained using the EPIC-pn data during its current spin-up phase showed dips. Unlike other flaring sources like LMC X–4 and SMC X−1, it is interesting to notice a broad dip in the light curve soon after the decay of a large flare. This feature is similar to that observed in the bursting pulsar, GRO J1744−28. The light curve of GRO J1744−28 showed the presence of a dip and recovery period following each outburst (see e.g. Giles et al. 1996) and the X-ray spectrum of GRO J1744−28 showed no significant change going from quiescence to outburst (Cannizzo 1996). The same authors proposed that the outbursts observed in the bursting pulsar could be due to Lightman–Eardley instability (Lightman & Eardley 1974) in the accretion disc and the material that is evacuated on to the pulsar during an accretion event is replenished by material

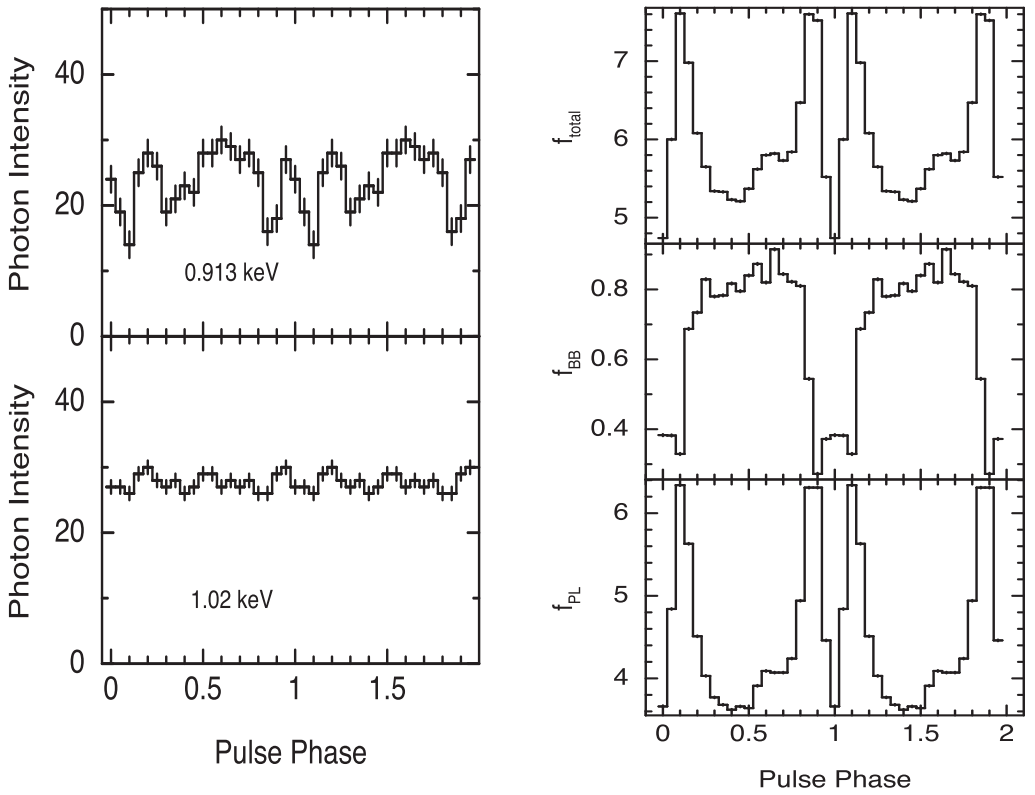

Figure 7. Variation of line flux across the pulse phase is plotted in left while the plot in right shows the variation of continuum flux with pulse phase. Line fluxes are in units of 10^{-4} photons cm^{-2} s^{-1} while all the continuum fluxes ($f_{\rm total}$, $f_{\rm BB}$, $F_{\rm PL}$) are measured in 10^{-10} erg cm^{-2} s^{-1}. All the errors are quoted with 1σ confidence.

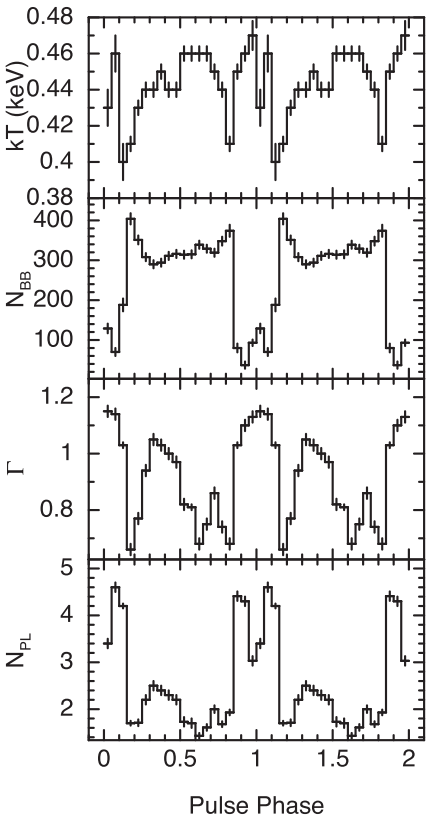

Figure 8. Variation of continuum parameters across the pulse phase.

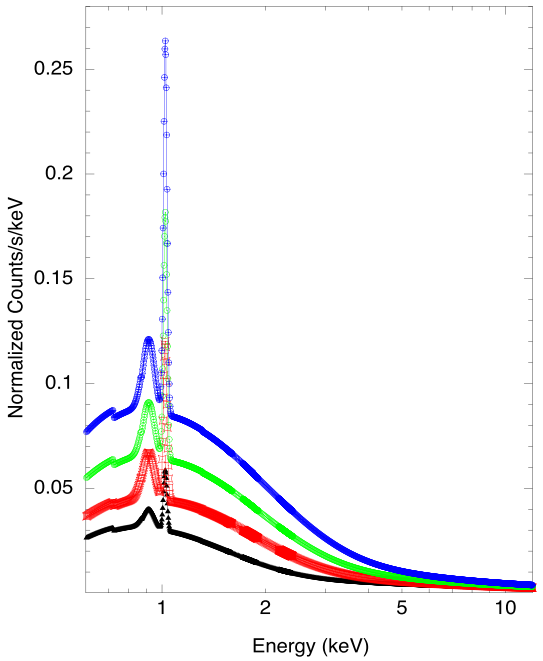

Figure 9. Best-fittingmodel components for intensity-resolved spectra. Blue colour represents the spectrum created using an intensity range of 200–320 counts s^{-1}, green: 150–200 counts s^{-1}, red for 90–100 counts s^{-1}, and black for spectrum during dip. From the figure, it is clear that normalization varies with the change in intensity.

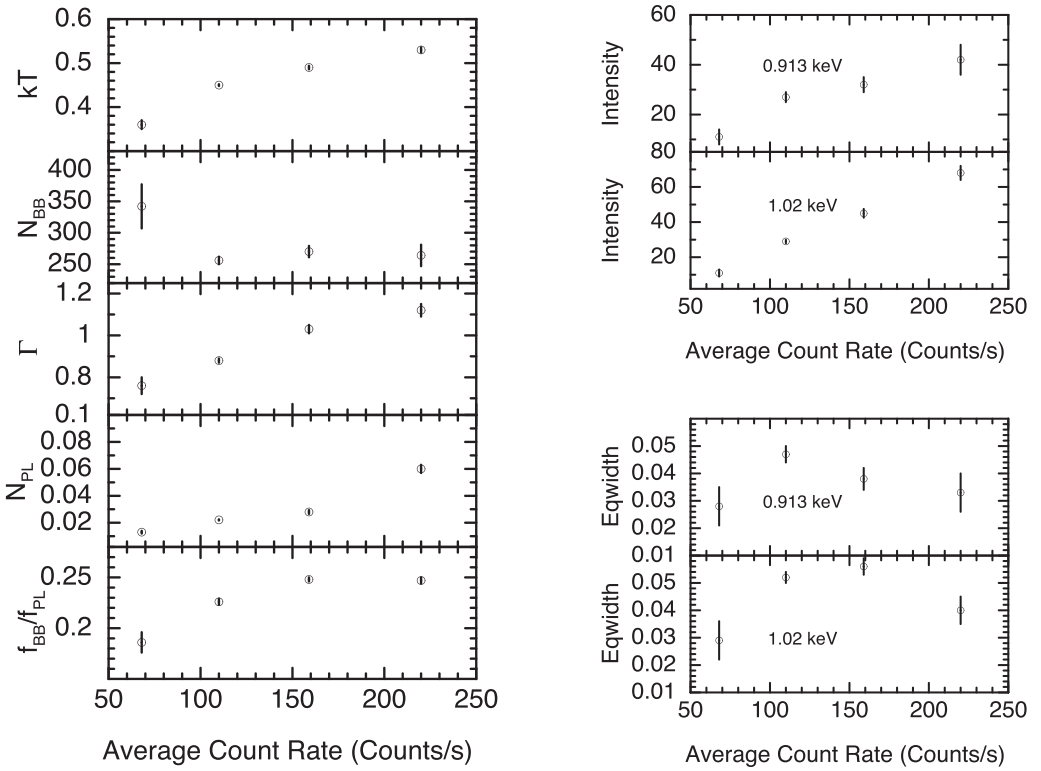

Figure 10. Left-hand plot shows the variation of continuum parameters with the increase in intensity, while the bottom panel of this plot shows the variation of ratio of blackbody flux and the power-law flux. On the right: top plot shows the variation of line flux with the increase in intensity. Line fluxes are in units of 10^{-4} photons cm^{-2} s^{-1} while the bottom plot shows the variation of EW of Ne IX and Ne X emission lines with the increase in intensity. Note: *X*-axis label refers to average count rate during different intensity-resolved spectra. All the errors are quoted with 1σ confidence.

flowing in from further out; hence, the dip and recovery in the light curve following an outburst. After performing intensity-resolved spectroscopy of 4U 1626−67, we found that overall there is no change in the shape of shape of the spectrum (see Fig. 9) except that the continuum and line parameters follow an increasing trend with intensity. Therefore, it is plausible that a similar mechanism might be responsible for the presence of flares and sharp dips in the light curve of 4U 1626−67.

(ii) A QPO feature around 3 mHz is observed in the PDS. This feature has been observed for the first time using X-ray data of current spin-up phase. The feature at 3 mHz also shows strong energy dependence. The feature is sharp at low energies as flares dominate at low energies.

The energy dependence of fractional rms amplitude of a QPO has been used as a tool to understand the physical origin of the QPO (see e.g. Gilfanov, Revnivtsev & Molkov 2003; Cabanac et al. 2010; Mukherjee & Bhattacharyya 2012). The fractional rms amplitude of a 3 mHz QPO observed in 4U 1626−67 showed an increase up to 5 keV and thereafter its value saturates (probably due to lower count rates at higher energies). Therefore, it seems that fluctuations in the blackbody component could be a plausible cause of the observed mHz QPO in 4U 1626−67.

(iii) We found that the pulse profile shape below 2 keV is different from that seen during spin-down phase of 4U 1626−67 (Fig. 4). Moreover, during its spin-up phase, pulse profiles below 2 keV are quite different from that seen above 2 keV (Fig. 3). A possible explanation to these observations is changes in the emission diagram of the accretion column. During the low-luminosity phase (spin-down) of 4U 1626−67, the emission of the accretion column is concentrated in a beam, oriented along the magnetic field axis while during the high-luminosity phase (spin-up) the emission diagram changed to the fan beam pattern (Basko & Sunyaev 1975). Soft X-ray emission (below 2 keV) is attributed to reprocessing of the primary emission by the optically thick material (i.e. the inner accretion disc) and, therefore, changes in the emission diagram might lead to the changes in the illumination of the inner accretion disc and hence, different pulse profiles below 2 keV during the spin-up phase compared to the spin-down phase of 4U 1626−67. We also note that the similar hypothesis was also proposed by Koliopanos & Gilfanov (2016) to explain the origin of the iron line during the spin-up phase.

(iv) Values of EW of emission lines observed in the phase-averaged spectrum suggest that the EW of O VIII has increased by a factor of 4 compared to the value (∼7 eV) measured with *Suzaku* during its spin-up phase by Camero-Arranz et al. (2012). However, EW measured with *ASCA* and *XMM–Newton* during its spin-down phase was ∼14 eV (Angelini et al. 1995; Krauss et al. 2007). Observations made with *ASCA* and *XMM–Newton* during the spin-down phase of 4U 1626−67 revealed EW of O VII to be ∼31 eV and ∼23 eV, respectively (Angelini et al. 1995; Krauss et al. 2007) while the measurement made during the spin-up phase with the *Suzaku* observatory showed a much lower value (1.3 eV). EWs of Ne IX and Ne X emission lines are almost consistent with the previous measurements made during its spin-up phase (Camero-Arranz et al. 2012).

(v) From the intensity-resolved spectroscopy, we found that there is an increase in the ratio between blackbody and power-law flux which suggests that the spectrum softens with the intensity. The

Table 3. Radius measurement for the Ne/O line-forming region.

Ion species	Radius[a] (spin-down)	Radius[a] (spin-up)
O VII	2.3	4.2
O VIII	1.4	2.6
Ne IX	1.2	2.1
Ne X	0.07	0.14

Note.[a]Radius measurements are in units of 10^{10} cm.

values of line fluxes at 0.913 keV and 1.02 keV also showed an increase with intensity. However, we did not notice any correlation between the EW of these emission lines with the intensity (Fig. 10).

(vi) From the pulse-phase-resolved spectroscopy of 4U 1626−67, we observed a strong variation of Ne IX emission line with the pulse phase while the emission line at 1.02 keV (Ne X) showed a lack of pulsations. A different behaviour of Ne IX and Ne X emission lines across the pulse phase suggests that these emission lines might have a different origin. It may be possible that the Ne IX emission line originates from the accretion disc and thus, showing a strong pulse phase dependence while the Ne X emission line originates from highly ionized optically thin emission, i.e. from the material trapped in the Alfvén shell (Basko 1980). If this scenario is true, it also provides an explanation to the different line shapes of Ne IX and Ne X emission lines. The broadening observed in the profile of the Ne IX emission line could be due to the Doppler shifts while the microscopic processes may be the cause of the broadening of the Ne X emission line.

Current observation made during spin-up phase of 4U 1626−67 showed a different line intensity modulation pattern of Ne IX emission line compared to the earlier *XMM–Newton* observation in the spin-down phase. Pulse phase dependence of low-energy emission lines in 4U 1626−67 is believed to be due to the geometrical effect called 'warping' of the accretion disc (Beri et al. 2015). Due to warps (wherein the tilt angle of the normal to the local disc surface varies with azimuth) in the accretion disc, one expects to observe modulation in the flux of reprocessed emission visible along our line of sight. Several possibilities have been discussed in the literature that might lead to warps in the accretion disc. One of the widely accepted possibility is that if the accretion disc is subject to strong central irradiation, then it is unstable to warping (see e.g. Petterson 1977; Pringle 1996). We also note that Pringle (1996) suggested that radiation-driven warping is strongest in the outer regions of the accretion discs. From Table 2, it is interesting to notice that O VIII emission line at 0.653 keV showed a lower value of velocity compared to the values measured during the spin-down phase of 4U 1626−67. This indicates that the radius of the accretion disc at which this emission line is formed has moved outward during the spin-up phase.

In order to further investigate the above, we estimated radii of Ne/O emission line-forming regions using the expression for ionization parameter ($\zeta = L_X/nR^2$), where L_X is the X-ray luminosity, n is the ion number density, and R is the radius (see Table 3) The values of ionization parameters calculated using the XSTAR code (Kallman & McCray 1982) for the optically thin photoionized model[2] were opted for our calculations. We further assumed a constant value (10^{13} cm^{-3}) for the electron number density. This is a reasonable assumption as comparable values of number density were estimated by Schulz et al. (2001). It is interesting to notice from Table 3 that the radius of line-forming region for each of the ion species has moved outwards compared to the values obtained using L_X measured during spin-down phase. This further supports our interpretation that a strong variation of Ne IX line during the current spin-up phase of 4U 1626−67 is because the structures (or warps) in the accretion disc (that produce pulse phase dependence of emission lines) have changed during its spin-up phase or the line-forming region has moved outwards where the warps dominate.

Different pulse phase dependence of Ne IX emission line observed during current spin-up phase of 4U 1626−67, therefore, supports that there is a possible change in accretion flow geometry. The accretion flow geometry plays an important role in transfer of angular momentum and therefore any change in it would suggest a change in the interaction between the Keplerian disc and the stellar magnetic field at the corotation radius.

[2] http://heasarc.gsfc.nasa.gov/lheasoft/xstar/xstar.html

ACKNOWLEDGEMENTS

We thank the anonymous referee for several useful suggestions which improved the quality of the paper. AB gratefully acknowledges Raman Research Institute (RRI) for providing local hospitality and financial assistance, where this work was started. She is also grateful to the Royal Society and SERB (Science and Engineering Research Board, India) for financial support through Newton-Bhabha Fund. AB would like to extend further thanks to Michael Smith and Matteo Guainazzi for their useful insights about *XMM–Newton* data analysis. We would like to thank all the members of the *XMM–Newton* observatory for carrying out observation of 4U 1626−67 during its current spin-up phase and for their contributions in the instrument preparation, spacecraft operation, software development, and in-orbit instrumental calibration.

REFERENCES

Angelini L., White N. E., Nagase F., Kallman T. R., Yoshida A., Takeshima T., Becker C., Paerels F., 1995, ApJ, 449, L41
Basko M. M., 1980, A&A, 87, 330
Basko M. M., Sunyaev R. A., 1975, A&A, 42, 311
Beri A., Jain C., Paul B., Raichur H., 2014, MNRAS, 439, 1940
Beri A., Paul B., Dewangan G. C., 2015, MNRAS, 451, 508
Cabanac C., Henri G., Petrucci P.-O., Malzac J., Ferreira J., Belloni T. M., 2010, MNRAS, 404, 738
Camero-Arranz A., Finger M. H., Wilson C., 2009, Astron. Telegram, 2099
Camero-Arranz A., Finger M. H., Ikhsanov N. R., Wilson-Hodge C. A., Beklen E., 2010, ApJ, 708, 1500
Camero-Arranz A., Pottschmidt K., Finger M. H., Ikhsanov N. R., Wilson-Hodge C. A., Marcu D. M., 2012, A&A, 546, A40
Cannizzo J. K., 1996, ApJ, 466, L31
Chakrabarty D., 1998, ApJ, 492, 342
Giles A. B., Swank J. H., Jahoda K., Zhang W., Strohmayer T., Stark M. J., Morgan E. H., 1996, ApJ, 469, L25
Gilfanov M., Revnivtsev M., Molkov S., 2003, A&A, 410, 217
Iwakiri W. B. et al., 2012, ApJ, 751, 35
Jain C., Paul B., 2009, Astron. Telegram, 2095
Jain C., Paul B., Joshi K., Dutta A., Raichur H., 2008, JA&A, 28, 175
Jain C., Paul B., Dutta A., 2010, MNRAS, 403, 920
Jansen F. et al., 2001, A&A, 365, L1
Joss P. C., Avni Y., Rappaport S., 1978, ApJ, 221, 645
Kallman T. R., McCray R., 1982, ApJS, 50, 263
Kaur R., Paul B., Kumar B., Sagar R., 2008, ApJ, 676, 1184
Kii T., Hayakawa S., Nagase F., Ikegami T., Kawai N., 1986, PASJ, 38, 751
Koliopanos F., Gilfanov M., 2016, MNRAS, 456, 3535
Kommers J. M., Chakrabarty D., Lewin W. H. G., 1998, ApJ, 497, L33
Krauss M. I., Schulz N. S., Chakrabarty D., Juett A. M., Cottam J., 2007, ApJ, 660, 605

Li F. K., McClintock J. E., Rappaport S., Wright E. L., Joss P. C., 1980, ApJ, 240, 628
Lightman A. P., Eardley D. M., 1974, ApJ, 187, L1
Middleditch J., Mason K. O., Nelson J. E., White N. E., 1981, ApJ, 244, 1001
Mukherjee A., Bhattacharyya S., 2012, ApJ, 756, 55
Orlandini M. et al., 1998, ApJ, 500, L163
Owens A., Oosterbroek T., Parmar A. N., 1997, A&A, 324, L9
Paul B., Nagase F., Endo T., Dotani T., Yokogawa J., Nishiuchi M., 2002, ApJ, 579, 411
Petterson J. A., 1977, ApJ, 216, 827
Pravdo S. H. et al., 1979, ApJ, 231, 912
Pringle J. E., 1996, MNRAS, 281, 357
Raman G., Paul B., Bhattacharya D., Mohan V., 2016, MNRAS, 458, 1302
Rappaport S., Markert T., Li F. K., Clark G. W., Jernigan J. G., McClintock J. E., 1977, ApJ, 217, L29
Schulz N. S., Chakrabarty D., Marshall H. L., Canizares C. R., Lee J. C., Houck J., 2001, ApJ, 563, 941
Strüder L. et al., 2001, A&A, 365, L18
Turner M. J. L. et al., 2001, A&A, 365, L27
van Kerkwijk M. H., Chakrabarty D., Pringle J. E., Wijers R. A. M. J., 1998, ApJ, 499, L27

This paper has been typeset from a TEX/LATEX file prepared by the author.